ADVANCES IN ATMOSPHERIC SCIENCES, 2026

• **Original Paper** •

Convection Initiation over Mountain Slopes in North China: Roles of Upslope Winds and Orographic Waves

Hongpei YANG[1], Yu DU[*1,2,3], Zijian CHEN[1], and Xiaoyu GAO[4]

[1]*School of Atmospheric Sciences, Sun Yat-sen University, and Southern Marine Science and Engineering Guangdong Laboratory (Zhuhai), Zhuhai, China*

[2]*Guangdong Province Key Laboratory for Climate Change and Natural Disaster Studies, Sun Yat-sen University, Zhuhai, China*

[3]*Key Laboratory of Tropical Atmosphere-Ocean System, Sun Yat-sen University, Ministry of Education, Zhuhai, China*

[4]*State Key Laboratory of Severe Weather Meteorological Science and Technology, Chinese Academy of Meteorological Sciences, Beijing, China*

(Received 30 August 2025; revised 8 December 2025; accepted 11 December 2025)

ABSTRACT

Using high-resolution observations, mesoscale simulations, and idealized experiments, this study investigates the mechanisms governing an episode of orographic convection initiation (CI) during the North China Heavy Rainfall Experiment. On 4 August 2024, repeated CI occurred over the eastern slopes of the Taihang Mountains in the late afternoon, subsequently enhancing an upstream downhill convective storm. Wind profiler radar data and dense automatic weather stations reveal that CI was supported by strengthening southeasterly upslope winds. These winds primarily resulted from the migration of the mountain–plain solenoid and the mountainward-propagating outflow from a convective cold pool over the plain, with sensitivity experiments showing the latter contributed roughly 22% of the wind strength. The upslope flows gradually transported unstable air from the plain to the slope, fostering CI. Mesoscale simulations further highlight the key role of orographic waves near the mountain ridge, which generated strong downslope winds. The near-surface convergence between downslope and upslope flows, combined with wave-induced divergence aloft, produced deep ascent over the slope. Removing mountain ridges weakened wave strength and reduced downslope wind speeds by ~8 m s^{-1}. Without orographic heating in the idealized simulation (i.e., no mountain–plain solenoid), only strong wave descent occurred below 2 km, inhibiting CI. These findings underscore the critical interplay among plain convection, orographic waves, and the mountain–plain solenoid, offering new insight into the processes controlling orographic CI in North China.

Key words: convection initiation, mountain–plain solenoid, orographic waves, cold pools, topographic convection

Citation: Yang, H. P., Y. Du, Z. J. Chen, and X. Y. Gao, 2026: Convection initiation over mountain slopes in North China: Roles of upslope winds and orographic waves. *Adv. Atmos. Sci.*, https://doi.org/10.1007/s00376-025-5589-9.

Article Highlights:

- Frequent CI occurred over the northeastern slopes of the Taihang Mountains ahead of the downhill storm in the late afternoon.
- Upslope winds intensified before CI through the combined effects of the mountain–plain solenoid and convective outflow from the plain.
- Convergence of the upslope winds and strong downslope winds induced by orographic waves favored CI over the slopes.

1. Introduction

Mountainous areas have long been recognized as hotspots for convection initiation (CI) (Bougeault et al., 2001; Lin et al., 2011; Smith et al., 2012; Bai et al., 2020). Once CI evolves into deep moist convection, it can produce precipitation and hazardous weather events, posing significant threats to public safety and property (Houze, 2012; Smith, 2019). Beacuse the accuracy of rainfall forecasts strongly depends on correctly predicting the timing and location of CI (Weckwerth et al., 2004; Geerts et al., 2017), advancing our understanding of orographic CI and improving its predictability are essential.

Mountainous terrain can trigger CI through multiple pathways. Dynamically, terrain-blocking effects can force air parcels to ascend over the windward slopes (Smith, 1979; Neiman et al., 2002), while terrain-induced flow splitting

* Corresponding author: Yu DU
Email: duyu7@mail.sysu.edu.cn

and detouring can generate convergence on the lee side (Mass, 1981), both of which can provide sufficient lifting for CI. Orographic waves may also be excited as airflow crosses mountain ranges, often generating downslope winds on the lee side (Klemp and Lilly, 1975; Durran, 1990). The associated warming and stabilization effects of these downslope winds typically suppress CI (Siler et al., 2013; Rojas and Minder, 2024).

Thermodynamically, CI can be driven by the mountain–plain solenoid (MPS) or mountain–valley breezes, induced by differential surface heating (Banta, 1990; Wolyn and Mckee, 1994). Daytime MPS circulation generates upslope winds and strong low-level convergence near or downstream of mountain ridges, favoring CI (Banta and Barker Schaaf, 1987; Weckwerth et al., 2011). At night, downslope flows may also converge with the ambient wind near the mountain base, but CI efficiency is generally low due to nocturnal stability (Kirshbaum et al., 2018). Importantly, different orographic mechanisms may act together, enhancing terrain forcing for CI (Banta, 1984; Kirshbaum, 2017).

North China, located at the transition zone between the second and third topographic steps of China, is a prime example of where complex terrain influences convection. The Taihang Mountains, with an average elevation exceeding 1000 m to the west, border metropolitan areas on the eastern flat plain. Radar observations show that many intense mesoscale convective systems (MCSs) over the North China Plain originate from upstream mountainous regions in the afternoon (Chen et al., 2012, 2014; Ma et al., 2021; Wu et al., 2023). These systems often undergo significant intensification while descending into the plain, both in storm intensity and spatial coverage (Chen et al., 2012; Xiao et al., 2017; Cheng et al., 2023). Since the propagation of MCSs relies on the initiation of new convective cells ahead of the MCS, these observations underscore the critical role of complex terrain in slope CI.

CI on the eastern flank of the Taihang Mountains is generally supported by favorable thermodynamic conditions and near-surface southeasterly flow. During the warm season, synoptic low-level jets frequently transport abundant moisture and unstable air into this region (Yu et al., 2007; Sun and Yang, 2008; Wilson et al., 2010). The southeasterly flow is strongly modulated by mesoscale circulations such as MPSs, urban heat island effects, and land–sea breezes. Among these, urban and sea-breeze circulations primarily contribute to precipitation over the North China Plain (Abulikemu et al., 2016; Xiao et al., 2017, 2019), whereas MPS-driven upslope flow (plain breeze) largely accounts for the afternoon precipitation peak along the mountain slopes (Yin et al., 2011; Bao and Zhang, 2013). However, due to the scarcity of high-resolution observations in mountainous regions, the detailed evolution of upslope winds and their role in CI, remain poorly understood.

Additional complexity stems from the interaction between upslope winds and other processes. For example, Gao et al. (2024) demonstrated that evaporative cooling from previous-day convective systems can reverse the typical mountain–plain thermal contrast, leading to daytime downslope breezes. Other studies have indicated that new CI can result from interactions between convective cold outflows and environmental winds (Feng et al., 2015; Jiang et al., 2025; Yang and Du, 2026). These findings suggest that pre-existing and surrounding convection strongly influences subsequent CI.

Another potentially important yet often overlooked factor is orographic waves. The high terrain in North China favors wave generation, but their impact on CI remains unclear. Hua et al. (2020), for instance, found that orographic waves forming under a stable nocturnal boundary layer produced adiabatic cooling, enhancing low-level humidity and preconditioning the environment for CI once upslope winds developed. Importantly, orographic wave characteristics vary with synoptic conditions and mountain geometry, resulting in different modes of interaction with upslope flows.

These gaps highlight the need to investigate the interplay between upslope winds, orographic waves, and surrounding convection, and how these processes jointly shape CI. This study addresses these issues by analyzing a case with frequent CI events over the slopes on 4 August 2024, during the first intensive observing period (IOP, June–September) of the North China Heavy Rainfall Experiment (NCHRE). Multiple sources of high-resolution observations and techniques were utilized during the NCHRE to improve the understanding and forecasting of heavy rainfall in the region. Section 2 outlines the event and mesoscale numerical simulation setup. Based on observations, section 3 investigates how the MPS and outflow of plain convection collectively enhance upslope winds. Section 4 demonstrates how upslope winds interact with orographic waves to favor CI, supported by both mesoscale and idealized simulations. Section 5 presents the results of sensitivity experiments designed to explore the roles of upslope winds and orographic waves in CI. Finally, section 6 summarizes the main findings and discusses implications for future research.

2. Case overview

2.1. *CI over mountain slopes*

On the afternoon of 4 August 2024, isolated convective cells initiated over the mountainous areas (Fig. 1a). While some of these cells quickly dissipated locally, others gradually organized and underwent upscale growth, developing into a quasi-linear MCS (MCS-M; Fig. 1b). Before propagating onto the eastern plain, the northern segment of MCS-M remained less organized and exhibited weaker radar reflectivity compared to its southern counterpart (Figs. 1c, d). Interestingly, during the downslope progression of MCS-M, frequent CI occurred along the eastern slopes of the Taihang Mountains ahead of MCS-M (Figs. 1c, d). These newly initiated cells merged with MCS-M, rapidly intensifying the northern portion of MCS-M, as reflected by a sharp increase in radar reflectivity (Fig. 1e). After descending the terrain, the north-

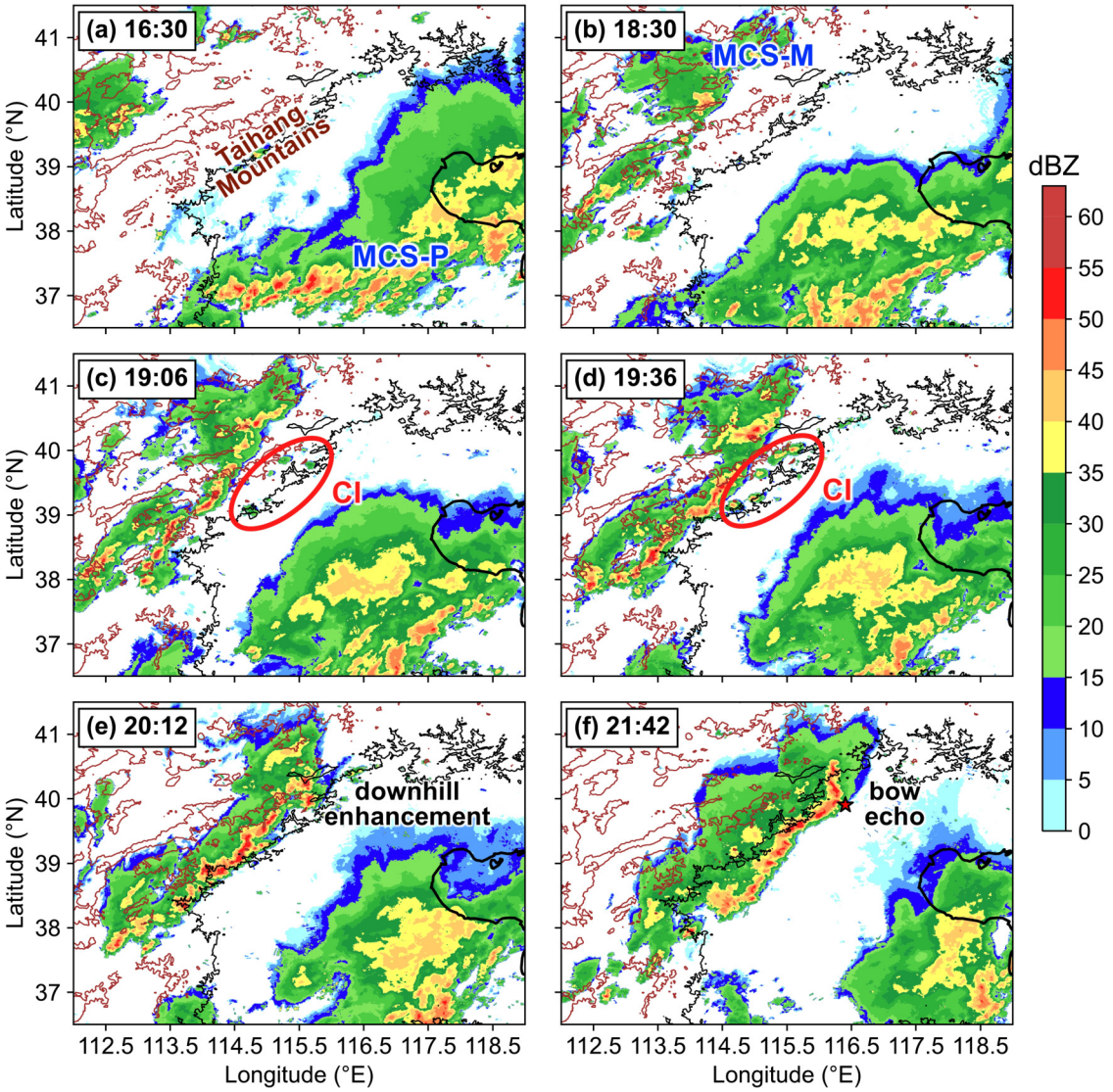

Fig. 1. Radar composite (shading; units: dBZ) on 4 August 2024 in North China, with topography contours at 500 m (black) and 1500 m (brown). The MCS over the plain (MCS-P) and the MCS over the mountain (MCS-M), which underwent downhill enhancement to become a bow echo, are labeled. The city center of Beijing is highlighted with a red star in (f). CIs over the mountain slopes are annotated with red ellipses and labels.

ern part of MCS-M, contrasting with the southern part, exhibited much higher reflectivity and evolved into a compact bow echo by 2142 LST (LST = UTC+8) (Fig. 1f). This mature MCS-M subsequently produced damaging winds and heavy rainfall, significantly impacting urban areas downstream. These observations highlight the critical role of slope CI in the downhill intensification of MCS-M, which constitutes the primary focus of this study.

Meanwhile, another extensive MCS (MCS-P) was present over the North China Plain during the evolution of MCS-M (Fig. 1a). By afternoon, its convective region had moved south of 38°N and continued propagating southeastward in the following hours (Fig. 1). However, its stratiform precipitation region expanded northwestward and persisted until 2000 LST (Figs. 1a–d). Around 1912 LST, the western edge of this stratiform region approached within 100 km of the slope CI area. Given the broad spatial extent and strong intensity of MCS-P, it likely generated a strong cold pool, potentially influencing CI through modifying local temperature and wind fields near the slopes.

2.2. *Synoptic background and strengthening upslope winds prior to CI*

Figure 2 shows the synoptic background three hours before CI, based on the ERA5 (fifth generation ECMWF atmospheric reanalysis) data. At 1600 LST, the CI area was situated ahead of a deep, westward-tilting upper-level trough (500–200 hPa), with a southwest–northeast-oriented shear line evident at 850 hPa, indicative of favorable large-scale ascent (Figs. 2a–c). In addition, CI occurred in the right-entrance region of an upper-level jet, where associated divergence further promoted upward motion (Fig. 2a). Meanwhile, northward penetration of the southwesterly monsoon, combined with terrain blocking, facilitated substantial mois-

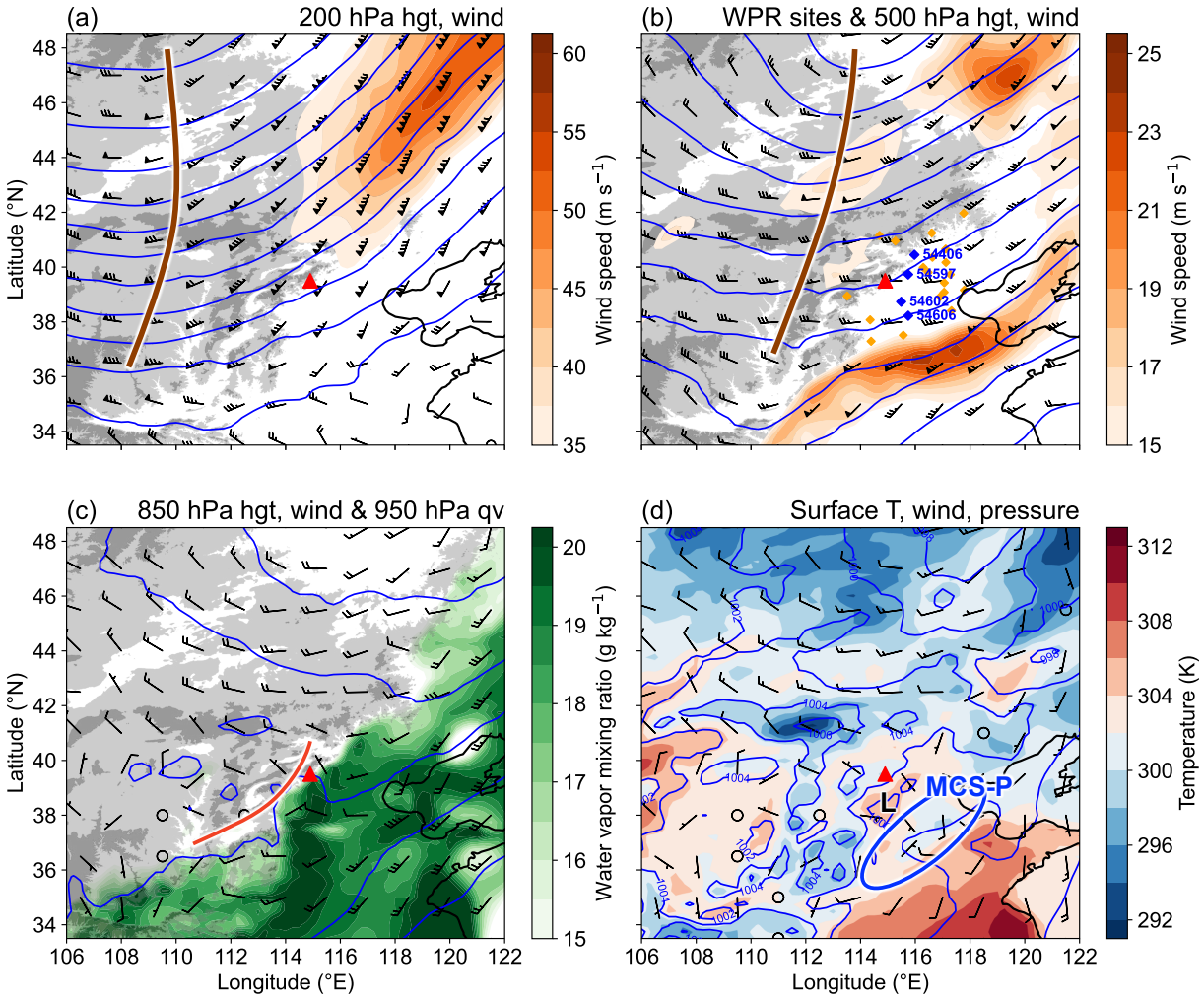

Fig. 2. ERA5 reanalysis fields showing the synoptic background at 1600 LST 4 August 2024. Geopotential height (blue contours; units: gpm), full wind speed (shading; units: m s^{-1}), and wind barbs at (a) 200 hPa and (b) 500 hPa, with brown lines denoting troughs. Diamonds in (b) mark WPR sites in North China, with the four radars used in Fig. 3 colored in blue and others in orange. (c) 850 hPa geopotential height (blue contours; units: gpm), wind barbs and shear line (red line), and 950 hPa water vapor mixing ratio (shading; units: g kg^{-1}). (d) 2 m temperature (shading; units: K), 10 m wind barbs, and mean sea level pressure (blue contours, hPa). The MCS-P is denoted by a blue ellipse and text, and "L" denotes a low-pressure center. A full wind barb represents 4 m s^{-1}, and a flag represents 16 m s^{-1}. The red triangles denote the CI area over the mountain slopes.

ture accumulation along the eastern slopes of the Taihang Mountains and across the North China Plain. This provided a thermodynamically favorable environment for CI and subsequent MCS development (Fig. 2c). Such synoptic patterns are typical for downhill MCS intensification in North China (Chen et al., 2014).

Near the surface, southeasterly winds blew toward the terrain (i.e., CI area), with a mesoscale low-pressure center ("L") over the foothills (Fig. 2d). This inflow was captured by multiple wind profiler radars (WPRs) during the IOP. As shown in Figs. 3a–c, all WPRs detected a marked strengthening of southeasterly winds after 1400 LST, indicated by a deepening easterly layer. Stations 54406 and 54602 also observed near-surface southeasterlies that peaked between 1800 and1900 LST, slightly prior to CI, consistent with the daytime migration of the plain breeze driven by the MPS.

ERA5 also indicated a local high-pressure zone with pronounced cold anomalies to the southeast, likely associated with MCS-P (Fig. 2d). The southern WPR station, 54606, detected westerly rear-inflow behind MCS-P as it passed during 1630–1730 LST (blue arrow in Fig. 3d). As MCS-P moved further southward, near-surface westerlies rapidly shifted to strong southerlies (>8 m s^{-1}) by ~1830 LST, possibly linked to convective cold outflow. Given the slope CI frequently occurred between 1900–2000 LST, the observed strengthening of southeasterlies suggests that enhanced upslope winds may have played a key role in triggering convection.

2.3. *WRF configuration and validation*

To complement observations, the Advanced Research version of the Weather Research and Forecasting (WRF-

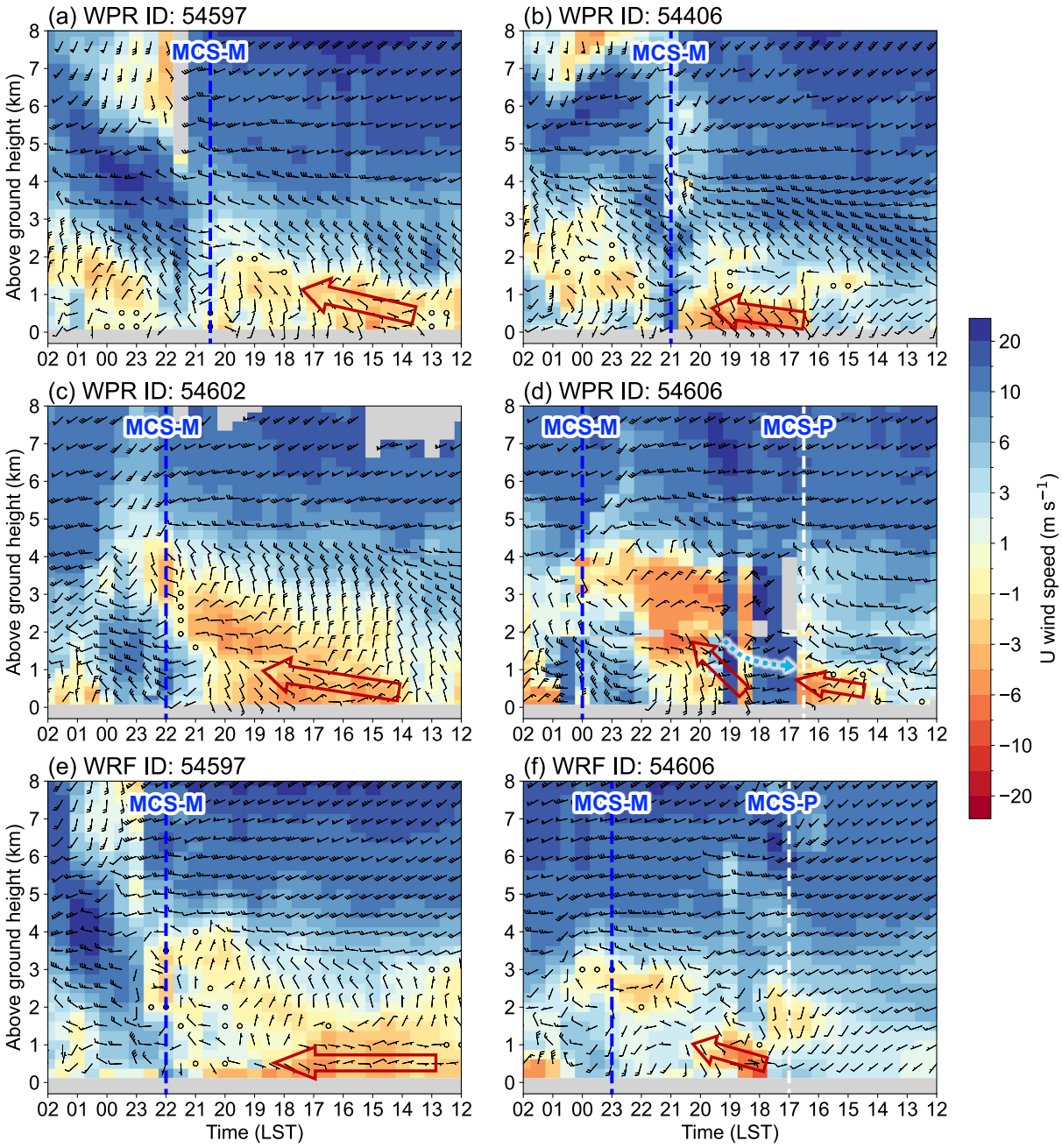

Fig. 3. Vertical profiles of horizontal wind barbs and U-wind speed (shading; units: m s^{-1}) from (a–d) four WPR sites (locations shown as blue diamonds in Fig. 2b), and (e, f) WRF-simulations at two WPR sites during 1200–0200 LST 4–5 August 2024. A full wind barb represents 4 m s^{-1}, and a flag represents 16 m s^{-1}. The passage of MCS-M is marked by blue dashed lines, while MCS-P is indicated by the white dashed line in (d, f). Red hollow arrows denote propagation of southeasterlies (upslope winds) and the blue arrow denotes the observed rear inflow of MCS-P.

ARW) model, version 4.2 (Skamarock et al., 2019) was employed to better investigate the potential interaction of upslope winds with other factors contributing to CI. A one-way nested setup with two domains was used (Fig. 4a), with horizontal grid-spacings of 9 km and 3 km, and 51 vertically stretched levels. The model was initialized at 0800 LST 4 August 2024 and integrated for 24 hours. Initial and boundary conditions were provided by the 0.25°, 6 h National Centers for Environmental Prediction Final (NCEP FNL) global analysis data. Physical parameterizations included the Thompson microphysics scheme (Thompson et al., 2008), Yonsei University planetary boundary layer scheme (Hong et al., 2006), the revised MM5 Monin–Obukhov surface layer scheme (Jiménez et al., 2012), the unified Noah land surface model (Livneh et al., 2011), and the Rapid Radiative Transfer Model for both longwave and shortwave radiation (Iacono et al., 2008). The Kain–Fritsch cumulus scheme (Kain, 2004) was adopted only in the outer domain.

As shown in Fig. 5, the control (CTL) run successfully reproduces the key features observed: the MCS-M over the

mountainous region, the MCS-P over the plain, and most critically, orographic CI along the eastern slopes of the Taihang Mountains. The simulated slope CI appears at nearly the same location as in observations (Fig. 1) and also features the concurrent initiation of multiple cells (Figs. 5c, d). A slight timing bias is noted, with CI simulated between 1800 and 1930 LST, approximately 0.5 to 1 hour earlier than observed. As will be discussed later, this discrepancy may be linked to biases in the simulated convection and associated cold outflow evolution over the plain.

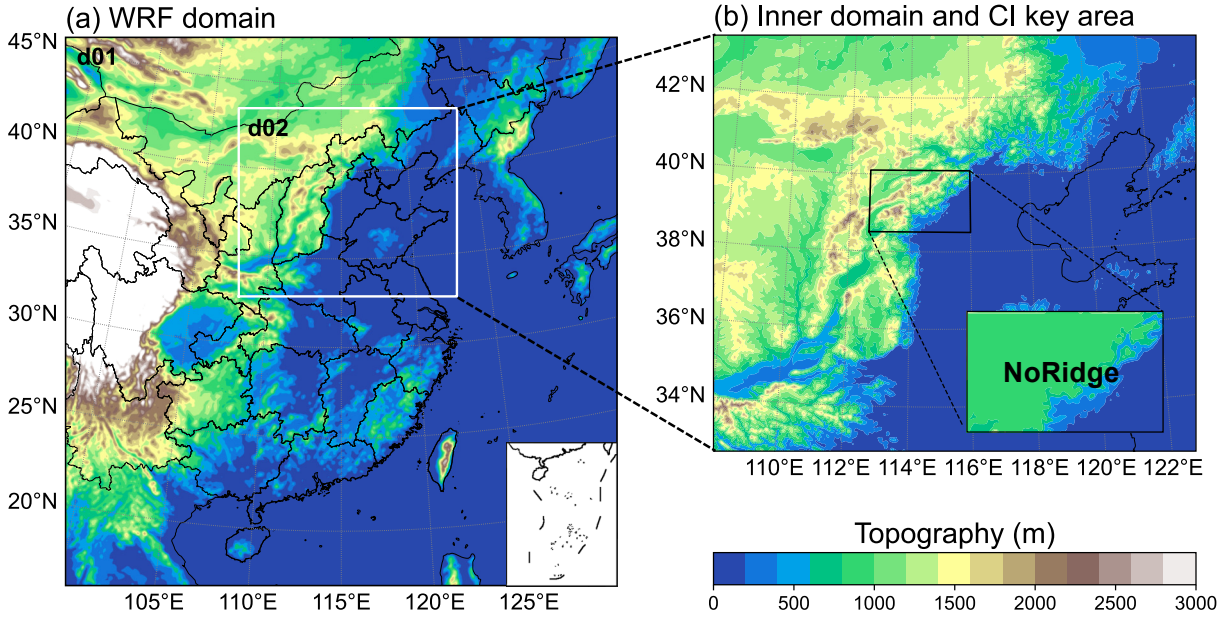

Fig. 4. (a) Domain configuration of the WRF model with two-nested domain. (b) Inner domain highlighting the CI key area (black box) and the terrain modification used in the NoRidge sensitivity experiment, where the ridges were removed.

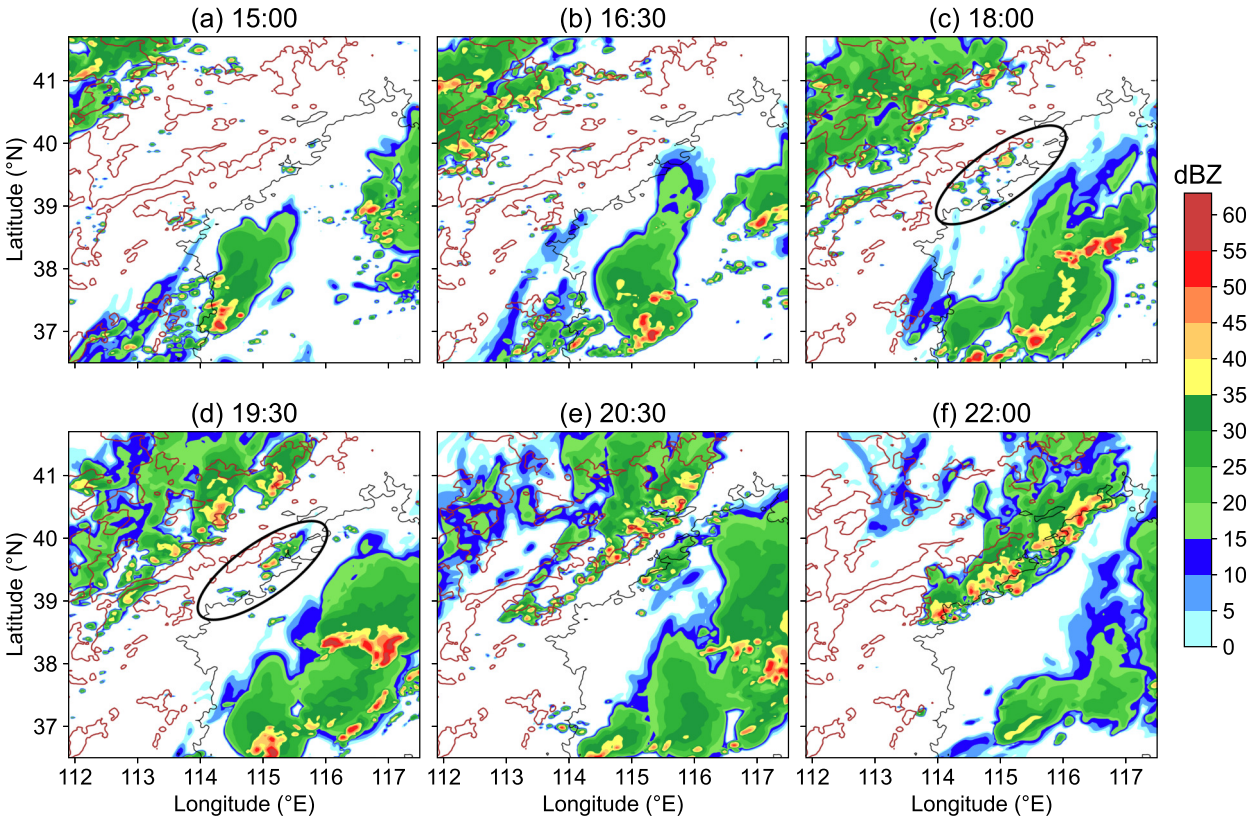

Fig. 5. WRF-simulated column maximum radar reflectivity (shading; units: dBZ) with topographic contours at 500 m (black) and 1500 m (brown) for the CTL experiment. Black ellipses denote the CI-active area.

Further validation was conducted using vertical wind profiles at grid points near two WPR stations: 54597 (closest to the CI area) and 54606 (recorded MCS-P passage). At 54597, the CTL run reproduces the pre-CI enhancement of southeasterly near-surface winds (Fig. 3e), consistent with WPR observations. At 54606, MCS-P is detected around 1700 LST in both observations and simulation, followed by a transition to strong southerlies after 1800 LST (compare Figs. 3d and 3f). Overall, the simulated spatiotemporal distribution of the CI and MCS, along with the evolution of near-surface winds, closely aligns with observations. This confirms that the CTL run provides a reliable basis for in-depth exploration of the CI mechanism and further quantitative sensitivity experiments.

3. Upslope winds amplified by two mechanisms

During the IOP, in addition to WPR observations, surface automatic weather stations (AWSs) along the eastern slopes of the Taihang Mountains also recorded pronounced southeasterlies, i.e., upslope winds (green boxes in Figs. 6a, b). The surface wind field was obtained by interpolating dense AWS data onto a 0.05° × 0.05° grid. The CTL simulation of WRF similarly reproduces this feature (Figs. 6c, d). Since the vertical component of the upslope winds is generally weaker than the horizontal component, our analysis focuses on the evolution of southeasterlies. As shown below, two mechanisms jointly contributes to the strengthening of upslope winds: the MPS and convective outflow.

3.1. *Migration of the MPS*

The MPS is a local circulation driven by thermal contrasts between mountains and plains. During the day, greater sensible heat release over mountain surfaces compared with the plains turns the mountains into an elevated heat source, inducing upslope winds. As shown in Fig. 6, both AWS observations and the CTL run reveal a clear near-surface potential temperature difference between the mountain and plain. This contrast intensifies after 1400 LST and becomes most prominent around 1800 LST (Figs. 7a, b). Concurrently, upslope wind speeds (u_s) also increase (Fig. 7b), reaching a maxi-

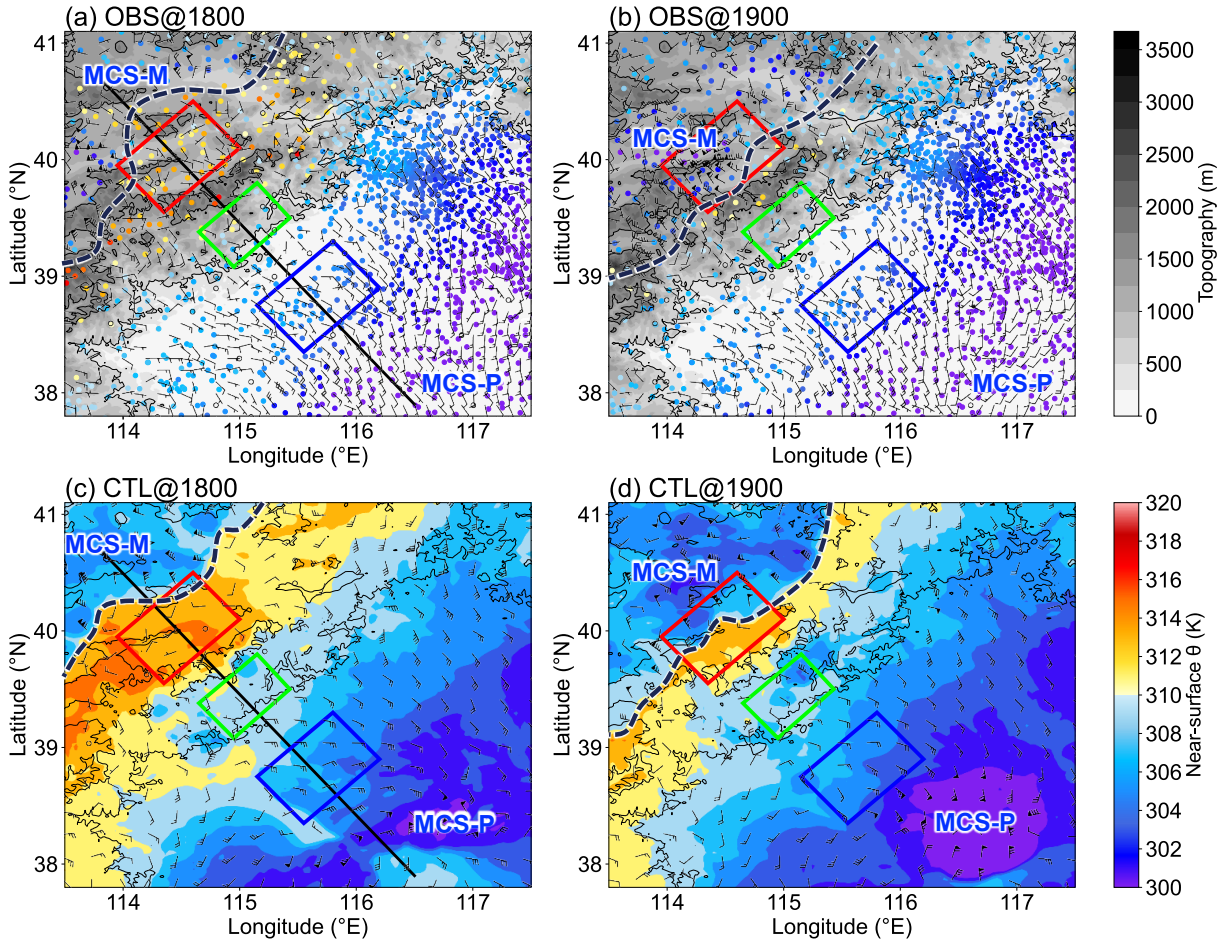

Fig. 6. (a, b) Surface observations of potential temperature θ (dots; units: K), 10 m wind barbs (AWS-observed winds, interpolated to a 0.05° × 0.05° grid), with terrain elevation (units: m) shaded. (c, b) WRF-simulated potential temperature (shading; units: K) and wind barbs at the lowest model level from CTL. A full barb represents 2 m s^{-1}, and a flag represents 8 m s^{-1}. Red, blue, and green boxes mark averaging areas for θ over mountain (mtn), plain (pln), and upslope winds (u_s, wind speed along the black line) in Fig. 7. Black dashed lines indicate the positions of the MCS-M gust front.

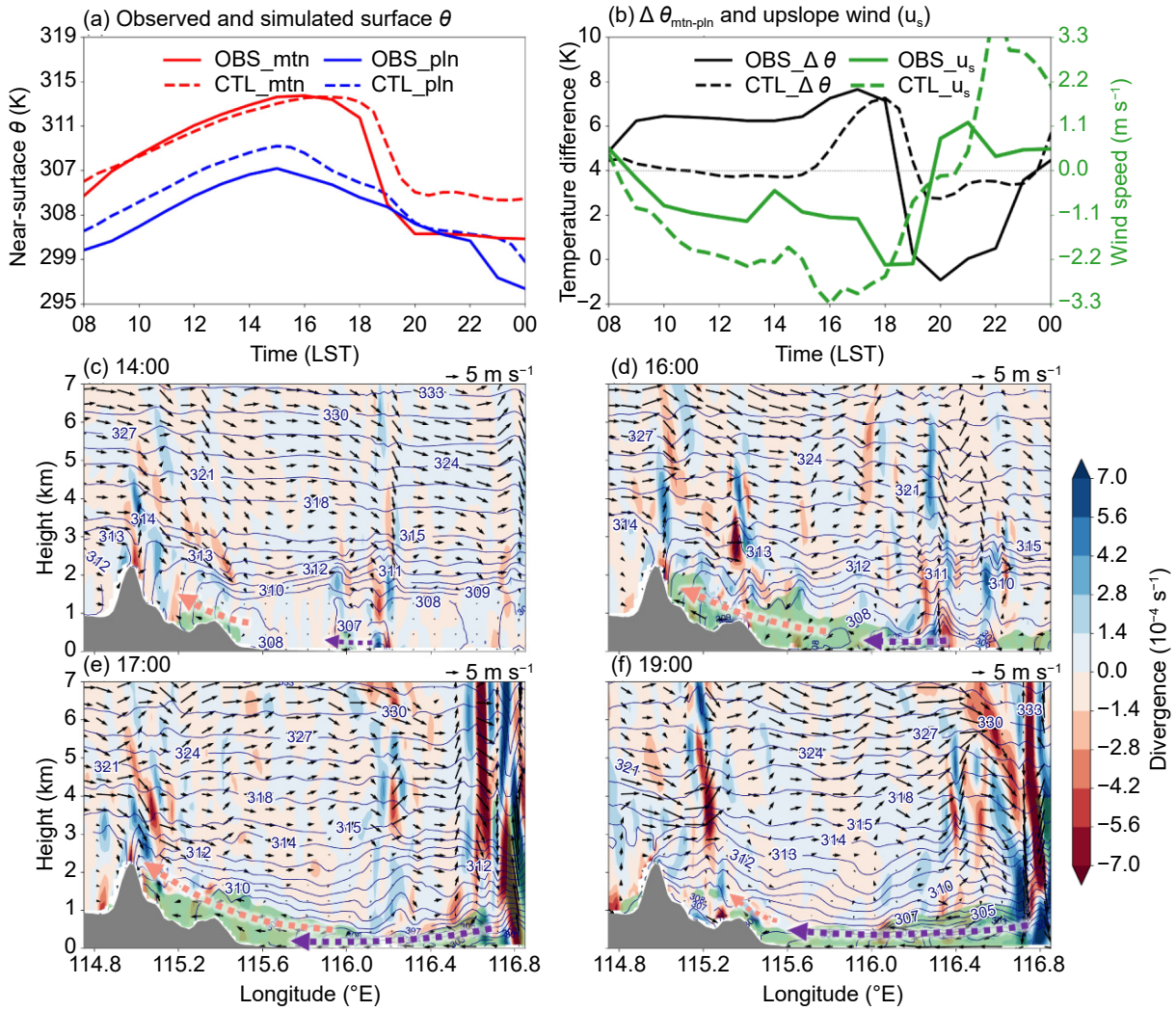

Fig. 7. Temporal evolution of (a) near-surface θ (units: K) and (b) the mountain–plain θ difference ($\Delta\theta_{\text{mtn-pln}}$) and upslope winds ($u_s$), comparing observations (solid) with CTL simulation (dashed). (c, d) Vertical cross-sections of CTL run divergence (shading; units: s^{-1}), potential temperature (contours; units: K), wind vectors (u_s and 10-times w), and upslope winds (green shading where >2 m s^{-1}) along the black line in Fig. 6a. Topography is indicated by gray shading, with the MPS and cold outflow denoted by pink and purple arrows, respectively.

mum of 5 m s^{-1} at 1800 LST in AWS observations (Fig. 6a). The synchronized growth of temperature contrast and upslope winds highlights the essential role of the MPS in preconditioning CI.

Figures 7c–f further illustrate the evolution of the MPS in the afternoon in the CTL run. The horizontal wind is projected onto the transect in Fig. 6, approximately perpendicular to the mountain orientation, with $u_s = -u\cos\alpha + v\sin\alpha$, where α is the transect angle from west. At 1400 LST, a shallow, localized upslope flow layer develops along the slope, associated with a distinct thermal circulation between the slope and the plain (green shading in Fig. 7c). Continued surface heating deepens and expands this flow layer, intensifying upslope winds (Figs. 7d, e). The upslope flow gradually occupies the entire eastern slope, spreading toward the mountain peak and propagating eastward toward the plain, consistent with the theoretical expectations (Wolyn and Mckee, 1994). Previous studies suggest that such upslope winds can favor CI near the mountain peaks through the strong low-level convergence they generate.

3.2. *Cold pool and associated outflow over the plain*

The surface potential temperature distribution highlights locally lower cooler air and sharp gradients over the plain (Figs. 7c, d), consistent with the earlier development of MCS-P as indicated by composite radar reflectivity (Fig. 2). In this case, the convective cold pool may enhance upslope winds through two pathways: (i) indirectly strengthening the mountain–plain thermal contrast, and (ii) directly superimposing its outward-propagating outflow onto the upslope flow.

Figures 7a and b show that near-surface potential temperature over the mountains continues to rise until ~1800 LST, when it drops rapidly upon the arrival of the MCS-M cold pool. In contrast, potential temperature over the plain decrease much earlier (1500 LST) due to the MCS-P cold

pool. This earlier cooling over the plain increases the mountain–plain thermal contrast and thereby amplifies upslope winds.

Meanwhile, both observed and simulated near-surface winds display flow spreading from the plain cold pool center toward the slopes (Figs. 7a, b). Vertical cross-sections confirm the presence of localized cold anomalies over the plain as early as 1400 LST (Fig. 7c). The evaporative cooling associated with the MCS-P precipitation significantly enhances the cold pool, evident from the denser isotherms. As a result, its surface outflow (southeasterlies) intensifies and directly superimposes and reinforces the MPS-driven plain breezes (Figs. 7d, e). In addition, the rearward expansion of this cold outflow, along with the southwestward movement of MCS-P, further broadens the coverage of southeasterlies around sunset (Figs. 7e, f).

Surface observations further confirm the interaction of the two airflows (outflow and MPS). Along the transect between the mountains and MCS-P, national AWSs (1 min temporal resolution) within 0.25° of the line were selected (Fig. 8a). As shown in Fig. 8b, the MPS first emerges over the mountains in the early afternoon, with southeasterly flow gradually expanding downslope toward the plain. Meanwhile, within the convective cold pool over the plain (indicated by low θ_e), southerly flow dominates initially, consistent with WPR observations (Fig. 3d). As the cold pool expands (with stratiform echoes in Fig. 2), its rear outflow strengthens and develops a more easterly component. This mountainward propagation persists until around 2000 LST when MCS-M descends the slope. The overlap between the two airflows begins between 1600 and 1700 LST, earlier than the frequent CI period (1900–2000 LST), suggesting that their interaction plays a key role in triggering CI. It is also notable that after 2000 LST, the further collision between the MCS-M outflow and the plain flows appears to contribute substantially to the subsequent intensification of MCS-M.

4. Downslope winds associated with orographic waves

Located to the west of the North China Plain, the Taihang Mountains have an average elevation exceeding 1000 m, providing a broad region for upslope wind development. However, both radar observations and WRF simulation reveal that CI is most active over the steeper slopes with the ridge exceeding 2000 m, particularly between 39° and 40° N near 115° E (Figs. 1 and 5). In addition, surface observations show that MCS-M had not yet crossed the ridge peak before 1900 LST (Figs. 1c and 6b), implying a limited impact of its outflow on CI. Therefore, the spatial preference of CI suggests a potential role of localized high terrain in modulating convection, most likely through the generation of significant orographic gravity waves.

4.1. *Convergence of upslope and downslope winds along the ridge*

As shown in Figs. 7a–c, the divergence field above the mountain peak near 115°E exhibits vertically alternating patterns and persists until CI onset, indicating orographic gravity waves. The divergence field averaged from 1400–1800 LST displays similar wave structures (Fig. 9a), while the phase lag between vertical velocity and potential temperature further confirms the notable vertical propagation of gravity waves from the mountain peaks toward the upper troposphere (not shown).

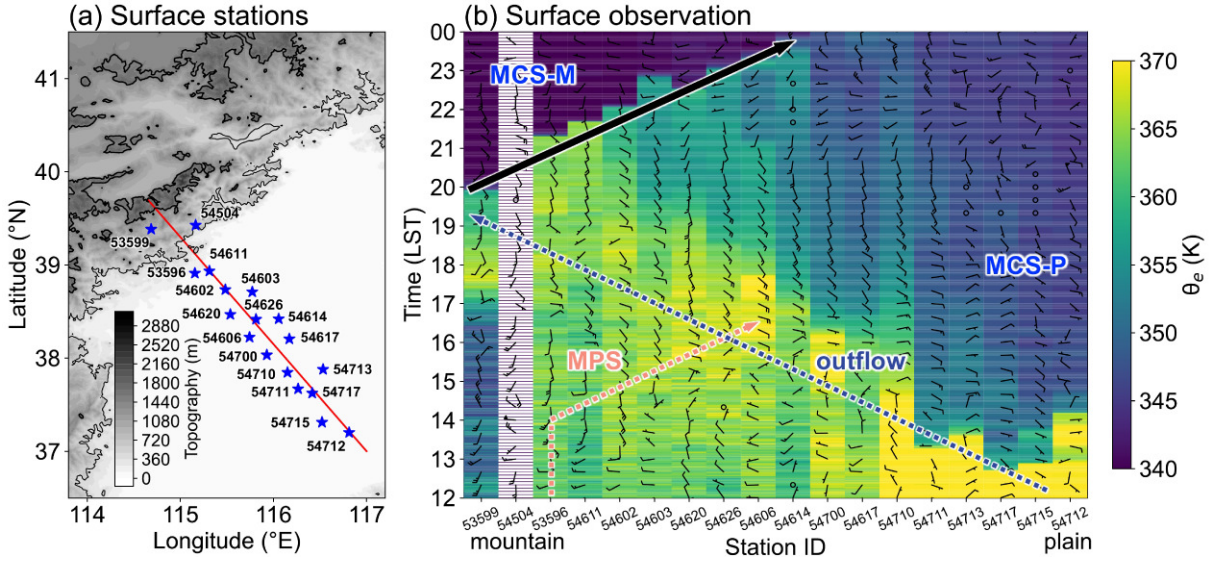

Fig. 8. (a) Topographic map showing selected surface stations (blue stars) along the red transect line, with elevation (shading; units: m) and contours at 500 m and 1500 m. (b) Hovmöller diagram of surface equivalent potential temperature (units: K) and 10 m wind barbs. A full line on wind barbs represents 2 m s^{-1}, and a flag represents 8 m s^{-1}. Pink and blue dotted arrows indicate the propagation of the MPS and cold pool outflow from the MCS-P, while the black arrow marks the downhill propagation of MCS-M.

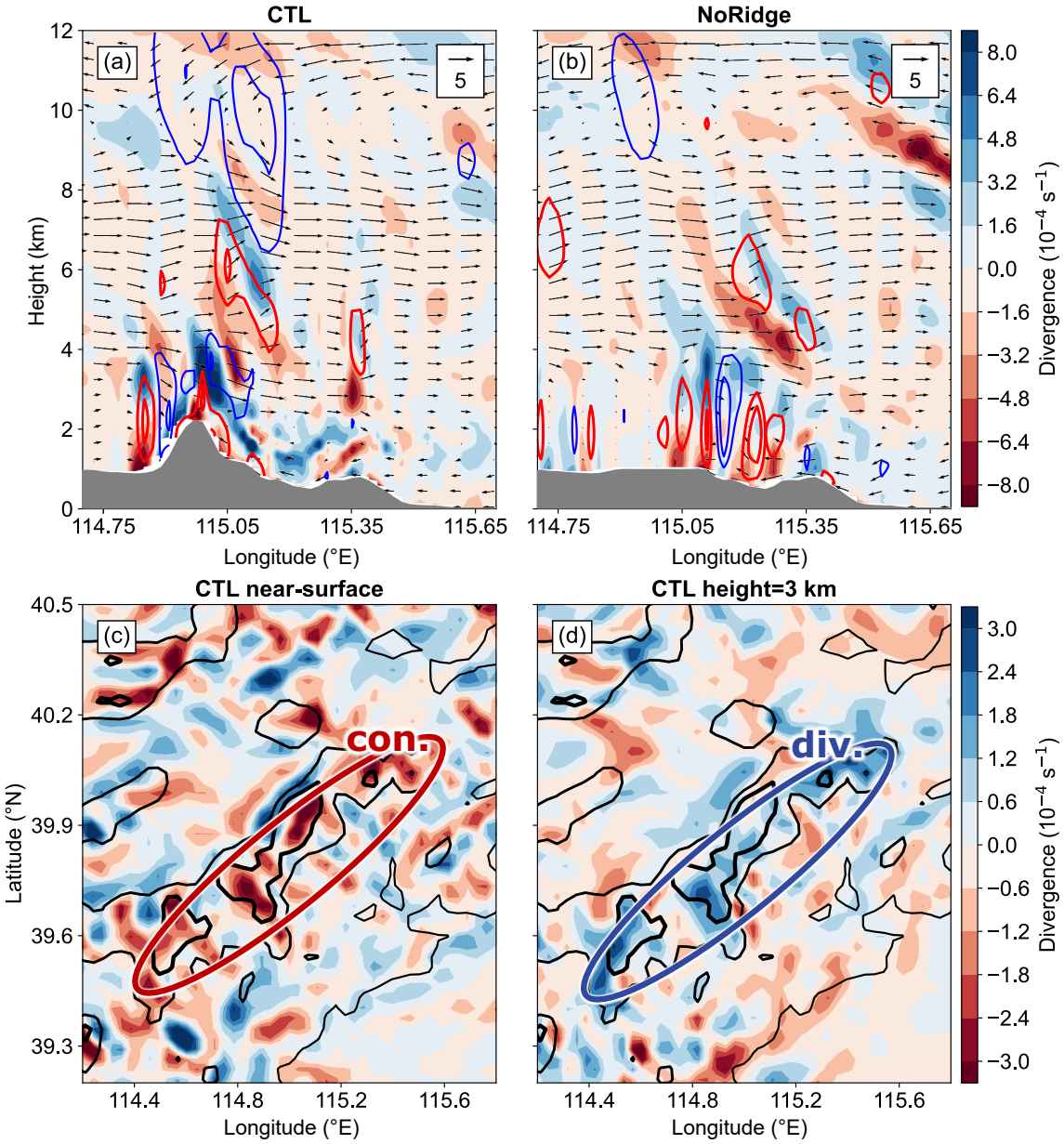

Fig. 9. Vertical cross-sections of time-averaged (1400–1800 LST) divergence (shading; units: s^{-1}), wind vectors (u_s and 10-times w), upward motions (red contours, 0.2, 0.4 m s^{-1}), and downward motions (blue contours, –0.4, –0.2 m s^{-1}) along the black line in Fig. 6 from the (a) CTL and (b) NoRidge experiments. The gray shading represents topography. Time-averaged divergence at (c) the near-surface level and (d) 3 km from the CTL run, with topography contoured in black at 500 m (thin) and 1500 m (bold). Ellipses highlight significant (c) near-surface convergence (con.) and (d) low-level divergence (div.) along the mountain ridge.

Classical theory predicts that gravity waves generated by high peaks produce strong downslope winds accompanied by near-surface divergence (Durran, 1990). In contrast, the CTL run indicates a near-surface convergence layer, while divergence and downslope winds are most pronounced between 2.5 and 4 km aloft (Fig. 9a). This discrepancy likely arises because idealized wave theory neglects thermal effects of topography, particularly the influence of upslope wind associated with the MPS. Indeed, both the CTL simulation (Fig. 9a) and surface observation (Fig. 6a) show small-scale downslope winds near the ridge peak, suggesting that the observed near-surface convergence arises from the interaction between enhanced upslope flow and the opposing downslope flow. Without this convergence, the mid–low-level divergence would typically suppress convection by inducing subsidence. Here, however, the coupling of near-surface convergence with overlying divergence produces a vertically continuous ascent from the surface to the middle troposphere (Fig. 9a), which is similar to the coupling of double low-level jets during heavy rainfall events (Du and Chen, 2019; Luo and Du, 2023). With a four-hour mean magnitude exceeding 0.2 m s^{-1}, this sustained upward motion can lift air

parcels by approximately 3 km, sufficient for them to reach the level of free convection, gain positive buoyancy, and trigger CI. Moreover, the horizontal distribution of divergence at different heights further confirms this mechanism: a persistent pattern of such coupling is evident along the mountain ridge (Figs. 9c, d), coinciding with the CI-active area (Figs. 2c, d). These results suggest that the interaction between upslope and downslope winds (orographic waves) is a crucial mechanism for CI in this case.

4.2. *Orographic waves over a heated mountain ridge*

To explicitly validate this intricate flow interaction, we further employ the idealized cloud model, CM1 (Bryan and Fritsch, 2002). Vertical wind and potential temperature profiles averaged along the transect during 1400–1800 LST from the CTL run are used as input to drive CM1 simulations (Fig. 10a). For wind, only upstream profiles are averaged to eliminate the influence of upslope flows. The mountain ridge is represented by the superposition of multiple Gaussian functions fitted to the actual terrain, following the approach of Hu et al. (2024). The 2D CM1 domain spans 600 km × 30 km with a horizontal grid-spacing of 3 km (consistent with WRF), and a vertical resolution of 200 m that was required to resolve the terrain. For simplicity, the simulations exclude the Coriolis force, moisture, and radiation. After a 72-h spin-up when orographic gravity waves reach quasi-steady state, the MPS is introduced in an idealized way by imposing a constant surface heating rate of 0.8 K h^{-1}.

The results highlight the contrasting roles of dynamic and thermal forcing. Without heating, CM1 reproduces classical orographic gravity waves generated by the ridge where the wave ascent is confined above ~2 km, and strong downslope winds (up to 11 m s^{-1}) dominate the slope (Fig. 10b). Such strong subsidence from downslope winds is unfavorable for CI. In contrast, when thermal forcing is included, the downslope wind zone weakens substantially (< 7 m s^{-1}), and upslope winds dominate the slope (Fig. 10c). The resulting convergence between upslope and downslope flows produces a deep column of ascent extending from the surface to ~5 km, closely resembling the CTL simulation (Fig. 9a) and directly supporting CI over the slope (Fig. 10c).

It is notable that, in addition to the pronounced alternating patterns of divergence (and w) near the peak, the CM1 simulations reveal a much broader wave influence on the horizonal wind field (Figs. 10b, c). This influence extends more than 100 km downstream of the ridge peak. For example, at the foothill (X = 100 km), the perturbation wind profiles evidently capture both the early quasi-stationary flow and the near-surface transition from downslope to upslope winds induced by heating (Fig. 11a). Similar behavior is evident in the CTL (Fig. 11b) and in observations from the two WPR sites near the mountains (Figs. 11c, d), although the exact wave modes differ due to the idealized nature of the CM1 configuration. Overall, these results demonstrate that the thermal forcing from the MPS and dynamic effects forcing from gravity waves interact, producing a strong topographic forcing, and thereby determining the location and timing of CI.

5. CI Sensitivities to mountain ridges and plain convection

In this section, we further employ the WRF simulations to examine the sensitivity of CI to both key mountain ridge and convection over the plain. In the NoRidge run, the mountain ridge corresponding to the CI-active region is removed to assess the role of localized high terrain (Fig. 4). In the HalfT experiment, the temperature feedback from the microphysics scheme is reduced by half, weakening MCS-P development and isolating the impact of its cold pool on slope CI.

5.1. *Changes in upslope and downslope winds*

We first examine changes in upslope wind evolution among the three experiments. As shown in Fig. 12a, compared to the CTL run, upslope winds in the HalfT run weaken by about 22% during 1600–1800 LST, whereas they strengthen markedly in the NoRidge run. Due to the suppression of microphysical temperature feedback in the HalfT run, only shallow convection develops over the plain (Figs. 12c, d), and the associated weaker cold pool outflow cannot reach the mountain slope (not shown). The near-surface temperature evolution shows that the absence of a cold pool allows higher temperatures to be maintained over both the mountain and plain than in CTL, with only a minor reduction in the mountain–plain temperature contrast (Fig. 12b). Thus, the weakened upslope winds in HalfT can mainly be attributed to the absence of outflow from the plain cold pool.

In contrast, in the NoRidge run, the removal of the mountain ridge allows MCS-M to organize more effectively over the mountain region (Figs. 12e, f). As a result, MCS-M can produce stronger cold pools, reducing the mountain–plain temperature contrast (Fig. 12b). However, this mechanism alone cannot explain the significantly enhanced upslope winds. Previous studies suggest that MCS-forced gravity waves may contribute to such enhancement (Wu and Lombardo, 2023; Yang and Du, 2024), but further investigation is warranted. Importantly, despite stronger upslope winds, CI does not occur along the slopes in NoRidge, highlighting the importance of orographic gravity waves in producing the near-surface convergence necessary for CI. Figure 9b shows that although the broader terrain in the NoRidge run still produces orographic waves, the near-surface field at the CI location is dominated by transient boundary-layer eddies without organized convergence. Finally, the CM1 experiment with the ridge removed also suggests that a high mountain peak is essential in generating large-amplitude orographic waves (downslope winds) and near-surface convergence (Fig. 10d).

5.2. *Changes in the thermodynamical environment*

In addition to dynamically generating near-surface convergence, the upslope winds precondition the local environment by advecting warm, moist air from the plain toward higher terrain. At 1400 LST, abundant moisture is present over the foothills and adjacent plain, in contrast to the rela-

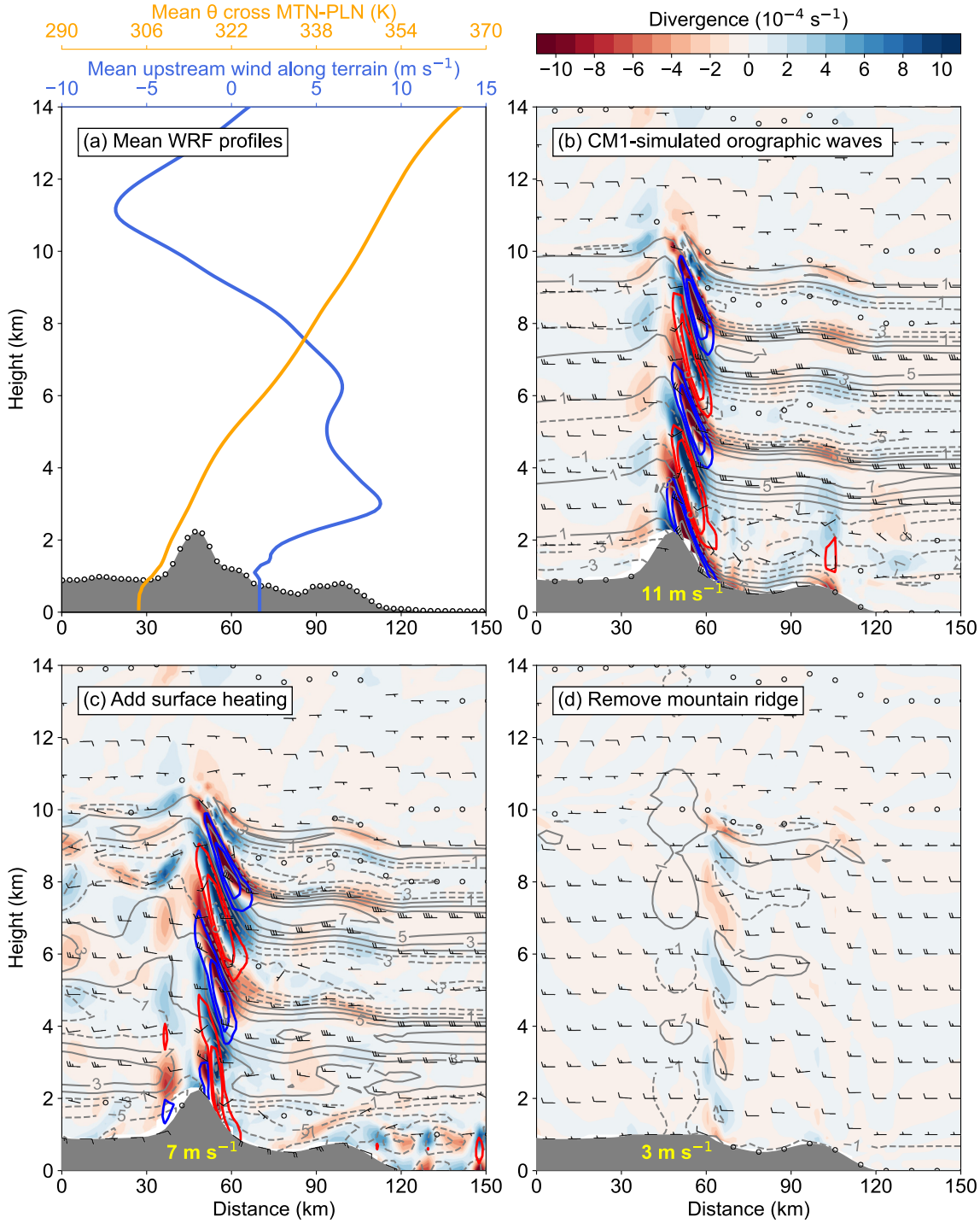

Fig. 10. (a) Mean upstream wind and the potential temperature profile derived from the CTL experiment, and the analytical terrain function (gray shading) fitted from the real topography (black-edged white dots) used to drive (b–d) three CM1 runs. (b–d) Vertical cross-sections of divergence (shading; units: s^{-1}), wind barbs (u and 10-times w), u-wind perturbation (gray contours; units: m s^{-1}), upward motions (red contours, 0.3, 0.6 m s^{-1}), and downward motions (blue contours, −0.6, −0.3 m s^{-1}) at 84 hours, with the gray shading representing the topography and the yellow text showing the maximum downslope wind speed near the ridge.

tively dry boundary layer near the mountain peak (Fig. 13a). This rich moisture supply supports strong instability, with CAPE exceeding 3000 J kg^{-1} but remaining much lower near the peak. During the subsequent four hours, the CTL run shows strengthened southeasterlies advecting moisture upslope (Figs. 13b, c). By 1800 LST, instability further increases at the foothills, but the most pronounced destabilization occurs along the slope. Near the mountain peak, the water vapor mixing ratio rises by 4–6 g kg^{-1}, while CAPE increases by roughly 1500 J kg^{-1}. This thermodynamic pre-

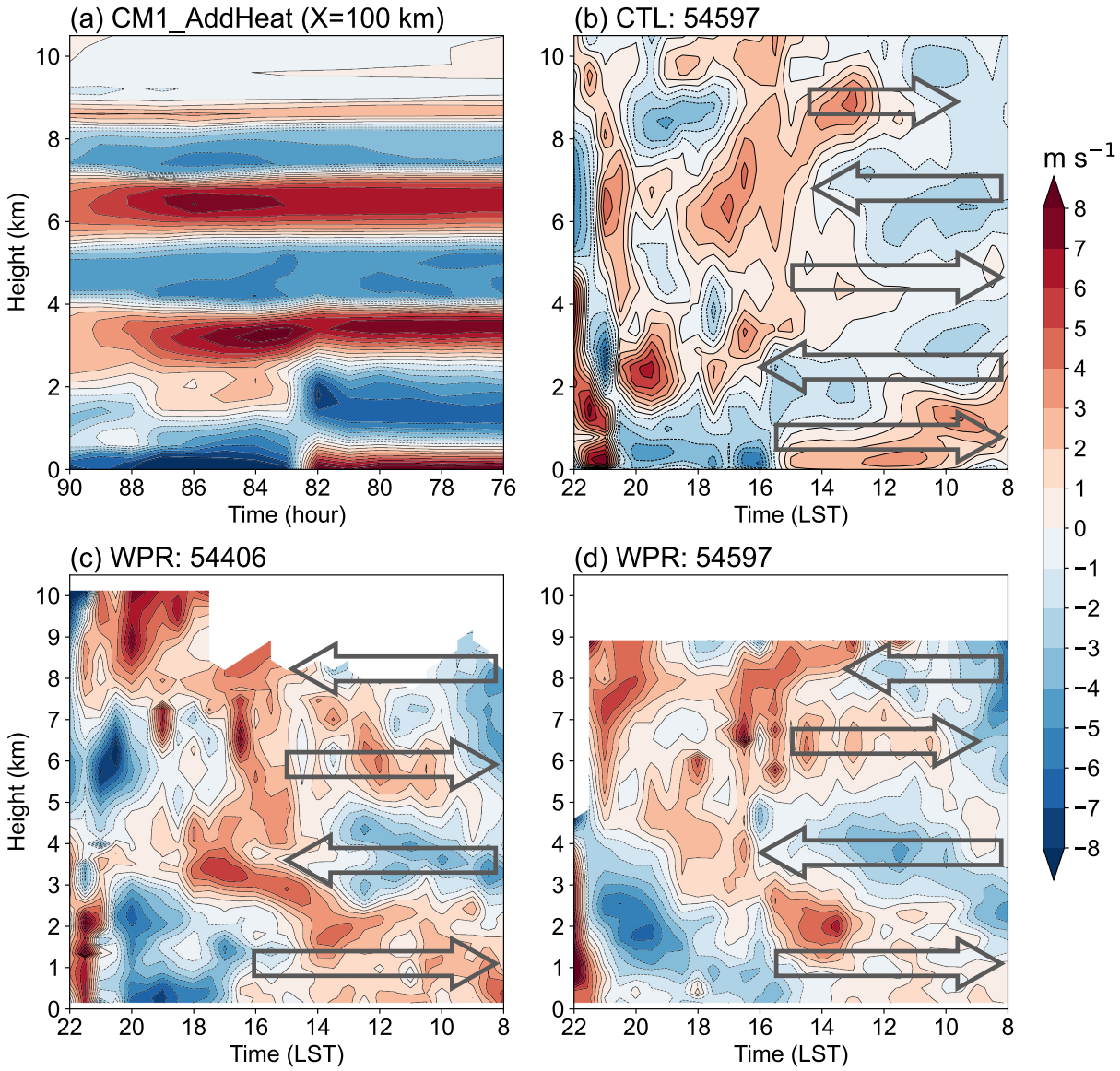

Fig. 11. Time–height diagrams of (a) u-wind perturbation from the CM1 run with heating at the foothill (X = 100 km in Fig. 10c), and (b–d) upslope-wind intensity anomalies relative to the 0800–2200 LST mean from (b) the CTL run at the grid point nearest WPR site 54597 and from WPR sites (c) 54406 and (d) 54597. Gray arrows in panels (b–d) denote the quasi-stationary wave-related flow.

conditioning effect is critical for supporting CI at higher elevations.

The evolution of the thermodynamic environment varies substantially in the two sensitivity experiments. In NoRidge, enhanced upslope winds transport warm, moist air more efficiently from the plain into the mountainous region (Figs. 13d–f), accelerating the earlier organization of MCS-M. By contrast, in HalfT, the artificial suppression of temperature feedback and convective development prevent depletion of moisture and instability over the plain. Consequently, once upslope winds develop, albeit weaker, they continue to advect unstable air onto the slopes, leading to larger instability (Figs. 13g–i). This explains the earlier appearance of weak convective echoes along the slopes (Figs. 13i–l). These results highlight the contrasting dynamical and thermodynamical roles of plain convection in slope CI, warranting further investigation in future studies.

6. Concluding remarks

In North China, rainfall events are strongly linked to topography. However, the roles and complex interactions of orographic forcings and other factors in convection initiation (CI) and subsequent storm evolution over the mountain slopes remain poorly understood. During the North China Heavy Rainfall Experiment (NCHRE), a CI episode was observed on the eastern slopes of the Taihang Mountains in the late afternoon of 4 August 2024, occurring most frequently between 1900 and 2000 LST on the leeward slopes of mountain ridges with peaks exceeding 2000 m. These slope CIs sub-

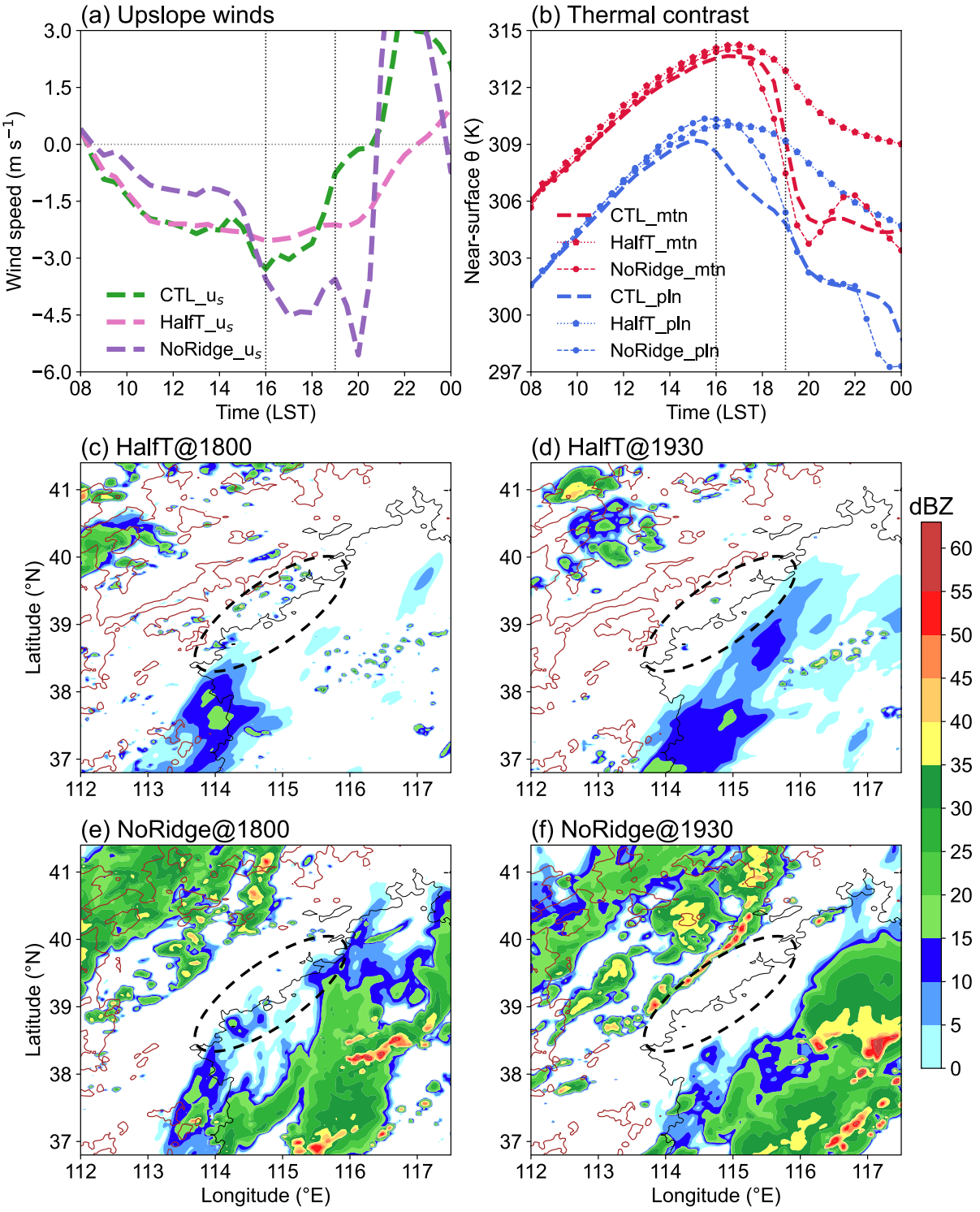

Fig. 12. Temporal evolution of (a) upslope winds (units: m s^{-1}) and (b) near-surface θ (units: K) over the mountain and plain regions for the three WRF experiments. Column-maximum radar reflectivity (shading; units: dBZ) with topographic contours at 500 m (black) and 1500 m (brown) for the (c, d) NoRidge and (e, f) HalfT experiment. Black ellipses denote the CI-active area in the CTL run.

sequently merged with an mesoscale convective system (MCS) originating from upstream mountains (MCS-M), intensifiying it and eventually evolving into a severe bow echo over the eastern plain. Notably, an earlier-developing MCS over the eastern plain (MCS-P) was also present prior to the slope CIs. Using high-resolution observations, along with WRF and idealized numerical simulations, this study identifies the primary factors contributing to CI and examines their interactions.

Surface station and wind profile radar data reveal a pro-

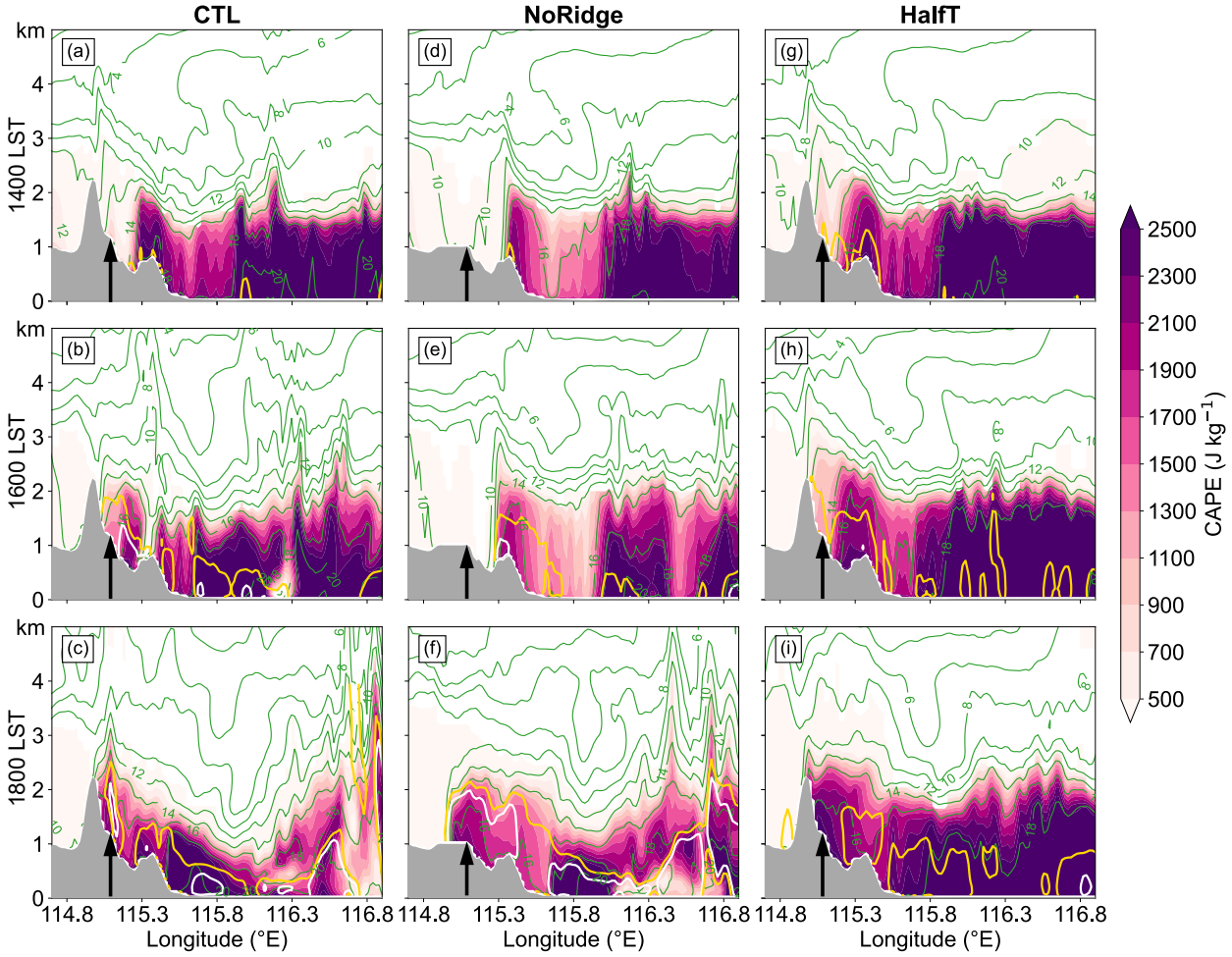

Fig. 13. Vertical cross-sections along the black line in Fig. 6 for the (a–c) CTL, (d–f) NoRidge, and (g–i) HalfT experiments, showing the CAPE (shading; units: J kg^{-1}), water vapor mixing ratio (green contours; units: g kg^{-1}), and upslope winds (yellow contours, 3 m s^{-1}; white contours, 5 m s^{-1}). Topography is shaded in gray, and black arrows indicate the CI location in CTL.

nounced enhancement of upslope winds prior to CI, driven by two mechanisms. The first is the mountain-plain solenoid (MPS), which arises from thermal contrasts between the mountains and the plain. During the afternoon, the increasing thermal contrast gradually strengthens the upslope winds and promotes the expansion of MPS circulation toward the plain. Over the slope, these upslope winds broaden, deepen, and intensify. The second mechanism is the outflow from the MCS-P cold pool, which generates divergent outflow propagating toward the mountains, reaching the foothills by 1700–1800 LST. Surface observations confirm that these two flows begin to superimpose around 1600 LST, thereby enhancing the upslope winds. WRF sensitivity experiments suggest that the cold pool outflow accounts for ~22% of the upslope wind strength.

This enhanced upslope flow supports CI by advecting unstable air from the plain to the slope and, more importantly, converging with downslope winds generated by high mountain ridges. The elevated peaks within the CI-active area favor the formation of strong orographic gravity waves under the influence of upstream winds, which induce pronounced downslope winds. While downslope winds typically inhibit CI through downward motions and drying, in this case their convergence with the amplified upslope winds promotes deep ascent. Coupled with wave-induced divergence in the mid–lower troposphere (2.5–4 km), this near-surface convergence drives deep ascent from the surface over the slopes, promoting CI. Idealized CM1 experiments that isolate the effects of gravity waves and the MPS, confirm this interaction, which is most prominent over terrain exceeding 1500 m, explaining the spatial preference of CI. Additional simulations with mountain ridges removed show a substantial weakening of both gravity waves and downslope winds, thereby reducing this interaction and suppressing slope CI.

These processes are summarized in the conceptual diagram shown in Fig. 14. Compared with previous studies, this work provides a detailed depiction of the fine-scale evolution of upslope winds and their controlling factors. It demonstrates that dynamic and thermal topographic forcings jointly influence the timing and location of CI. However, due to variability in terrain across North China, CI exhibits regional differences (Luo et al., 2020). For instance, in the northern regions near the east–west-oriented Yanshan Mountains, convective development is closely linked to low-level

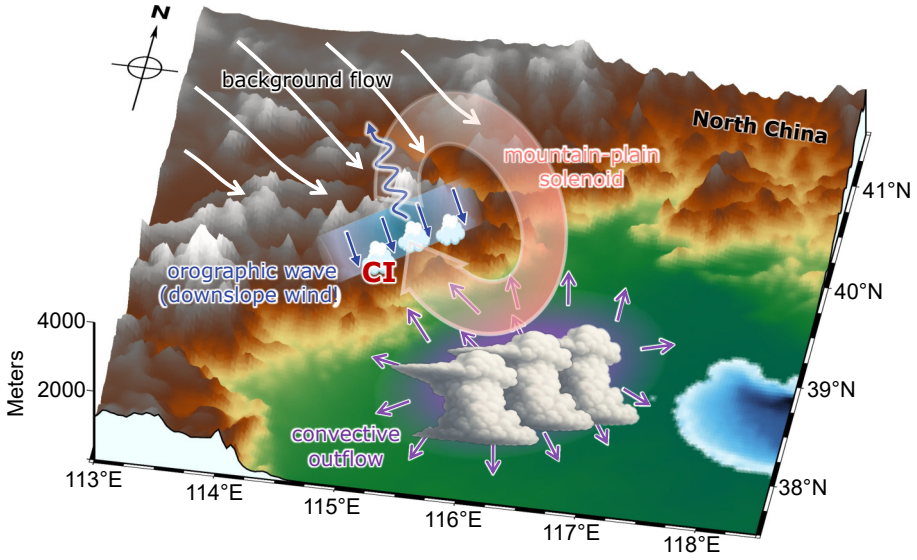

Fig. 14. Conceptual model of CI over mountain slopes in North China. CI results from the convergence between (1) downslope winds generated by orographic waves near ridges, and (2) amplified upslope winds driven jointly by the MPS and convective outflow from the plain, with the latter persistently advecting unstable air along the slope.

jets (Sun, 2005), whereas in the Beijing–Tianjin area near Bohai Bay, sea-breeze fronts and urban circulation are more influential (Sun and Yang, 2008; Abulikemu et al., 2016; Xiao et al., 2025). Therefore, targeted statistical investigations of CI across North China subregions are essential for identifying dominant mechanisms. Finally, understanding of orographic gravity waves and their interactions with other processes remains limited due to sparse observations over the mountains, particularly for vertical profiles. This study highlights that improved, targeted observations of orographic gravity waves might advance weather forecasting in the region.

Acknowledgements. This study was supported by the National Key Research and Development Program of China (Grant No. 2024YFC3013003), the National Natural Science Foundation of China (Grant Nos. 424B2033 and 42475002), projects supported by the Southern Marine Science and Engineering Guangdong Laboratory (Zhuhai) (Grant Nos. SML2024SP035, SML2024SP012, and 311024001), the Guangdong Project of Basic and Applied Basic Research (Grant Nos. 2024A1515510005 and 2025A1515011974), the Key Innovation Team of the China Meteorological Administration (Grant No. CMA2023ZD08), and the State Key Laboratory of Severe Weather Meteorological Science and Technology (Grant No. 2025QZA10). We also acknowledge the high-performance computing support from the School of Atmospheric Sciences of Sun Yat-sen University.

REFERENCES

Abulikemu, A., X. Xu, Y. Wang, J. F. Ding, S. S. Zhang, and W. Q. Shen, 2016: A modeling study of convection initiation prior to the merger of a sea-breeze front and a gust front. *Atmospheric Research*, **182**, 10–19, https://doi.org/10.1016/j.atmosres.2016.07.003.

Bai, L. Q., G. X. Chen, and L. Huang, 2020: Convection initiation in monsoon coastal areas (South China). *Geophys. Res. Lett.*, **47**, e2020GL087035, https://doi.org/10.1029/2020GL087035.

Banta, R. M., 1984: Daytime boundary-layer evolution over mountainous terrain. Part 1: Observations of the dry circulations. *Mon. Wea. Rev.*, **112**, 340–356, https://doi.org/10.1175/1520-0493(1984)112<0340:dbleom>2.0.co;2.

Banta, R. M., 1990: The role of mountain flows in making clouds. *Atmospheric Processes over Complex Terrain*, W. Blumen, Ed., American Meteorological Society, 229–283, https://doi.org/10.1007/978-1-935704-25-6_9.

Banta, R. M., and C. Barker Schaaf, 1987: Thunderstorm genesis zones in the Colorado Rocky mountains as determined by traceback of geosynchronous satellite images. *Mon. Wea. Rev.*, **115**, 463–476, https://doi.org/10.1175/1520-0493(1987)115<0463:tgzitc>2.0.co;2.

Bao, X. H., and F. Q. Zhang, 2013: Impacts of the mountain–plains solenoid and cold pool dynamics on the diurnal variation of warm-season precipitation over northern China. *Atmospheric Chemistry and Physics*, **13**, 6965–6982, https://doi.org/10.5194/acp-13-6965-2013.

Bougeault, P., and Coauthors, 2001: The MAP special observing period. *Bull. Amer. Meteor. Soc.*, **82**, 433–462, https://doi.org/10.1175/1520-0477(2001)082<0433:tmsop>2.3.co;2.

Bryan, G. H., and J. M. Fritsch, 2002: A benchmark simulation for moist nonhydrostatic numerical models. *Mon. Wea. Rev.*, **130**, 2917–2928, https://doi.org/10.1175/1520-0493(2002)130<2917:ABSFMN>2.0.CO;2.

Chen, M. X., Y. C. Wang, F. Gao, and X. Xiao, 2012: Diurnal variations in convective storm activity over contiguous North China during the warm season based on radar mosaic climatology. *J. Geophys. Res.: Atmos.*, **117**, D20115, https://doi.org/10.1029/2012JD018158.

Chen, M. X., Y. C. Wang, F. Gao, and X. Xiao, 2014: Diurnal evolution and distribution of warm-season convective storms in different prevailing wind regimes over contiguous North

China: Diurnal variations of convective storms. *J. Geophys. Res.: Atmos.*, **119**, 2742–2763, https://doi.org/10.1002/2013jd021145.

Cheng, W. J., X. D. Yu, X. M. Wang, and K. Li, 2023: Climatic characteristics of convective storms moving from Taihang mountains to North China Plain. *Meteorological Monthly*, **49**, 641–656, https://doi.org/10.7519/j.issn.1000-0526.2022.121201. (in Chinese with English abstract)

Du, Y., and G. X. Chen, 2019: Heavy rainfall associated with double low-level jets over southern China. Part II: Convection initiation. *Mon. Wea. Rev.*, **147**, 543–565, https://doi.org/10.1175/MWR-D-18-0102.1.

Durran, D. R., 1990: Mountain waves and downslope winds. *Atmospheric Processes over Complex Terrain*, W. Blumen, Ed., American Meteorological Society, 59–81, https://doi.org/10.1007/978-1-935704-25-6_4.

Feng, Z., S. Hagos, A. K. Rowe, C. D. Burleyson, M. N. Martini, and S. P. De Szoeke, 2015: Mechanisms of convective cloud organization by cold pools over tropical warm ocean during the AMIE/DYNAMO field campaign. *Journal of Advances in Modeling Earth Systems*, **7**, 357–381, https://doi.org/10.1002/2014MS000384.

Gao, X. Y., J. S. Sun, J. F. Yin, A. Abulikemu, C. Wu, X. D. Liang, and R. D. Xia, 2024: The impact of mountain-plain thermal contrast on precipitation distributions during the "23·7" record-breaking heavy rainfall over North China. *Atmospheric Research*, **310**, 107582, https://doi.org/10.1016/j.atmosres.2024.107582.

Geerts, B., and Coauthors, 2017: The 2015 plains elevated convection at night field project. *Bull. Amer. Meteor. Soc.*, **98**, 767–786, https://doi.org/10.1175/BAMS-D-15-00257.1.

Hong, S.-Y., Y. Noh, and J. Dudhia, 2006: A new vertical diffusion package with an explicit treatment of entrainment processes. *Mon. Wea. Rev.*, **134**, 2318–2341, https://doi.org/10.1175/MWR3199.1.

Houze, R. A., 2012: Orographic effects on precipitating clouds. *Rev. Geophys.*, **50**, RG1001, https://doi.org/10.1029/2011rg000365.

Hu, X. L., J. Li, H. M. Chen, and R. C. Yu, 2024: Diurnal off-mountain propagation of rainfall and low-level vertical velocity over the Lee side of the Yungui Plateau. *J. Atmos. Sci.*, **81**, 1963–1976, https://doi.org/10.1175/JAS-D-23-0145.1.

Hua, S. F., X. Xu, and B. J. Chen, 2020: Influence of multiscale orography on the initiation and maintenance of a precipitating convective system in North China: A case study. *J. Geophys. Res.: Atmos.*, **125**, https://doi.org/10.1029/2019jd031731.

Iacono, M. J., J. S. Delamere, E. J. Mlawer, M. W. Shephard, S. A. Clough, and W. D. Collins, 2008: Radiative forcing by long-lived greenhouse gases: Calculations with the AER radiative transfer models. *J. Geophys. Res.: Atmos.*, **113**, D13103, https://doi.org/10.1029/2008JD009944.

Jiang, X. L., D. L. Zhang, and Y. L. Luo, 2025: On the relay propagation of deep convection leading to a heavy rainfall event in a weak-wind urban environment. *Quart. J. Roy. Meteor. Soc.*, **151**, e4937, https://doi.org/10.1002/qj.4937.

Jiménez, P. A., J. Dudhia, J. F. González-Rouco, J. Navarro, J. P. Montávez, and E. García-Bustamante, 2012: A revised scheme for the WRF surface layer formulation. *Mon. Wea. Rev.*, **140**, 898–918, https://doi.org/10.1175/MWR-D-11-00056.1.

Kain, J. S., 2004: The Kain–Fritsch convective parameterization: An update. *J. Appl. Meteor.*, **43**, 170–181, https://doi.org/10.1175/1520-0450(2004)043<0170:TKCPAU>2.0.CO;2.

Kirshbaum, D. J., 2017: On upstream blocking over heated mountain ridges. *Quart. J. Roy. Meteor. Soc.*, **143**, 53–68, https://doi.org/10.1002/qj.2945.

Kirshbaum, D., B. Adler, N. Kalthoff, C. Barthlott, and S. Serafin, 2018: Moist orographic convection: Physical mechanisms and links to surface-exchange processes. *Atmosphere*, **9**, 80, https://doi.org/10.3390/atmos9030080.

Klemp, J. B., and D. R. Lilly, 1975: The dynamics of wave-induced downslope winds. *J. Atmos. Sci.*, **32**, 320–339, https://doi.org/10.1175/1520-0469(1975)032<0320:tdowid>2.0.co;2.

Lin, P.-F., P.-L. Chang, B. J.-D. Jou, J. W. Wilson, and R. D. Roberts, 2011: Warm season afternoon thunderstorm characteristics under weak synoptic-scale forcing over Taiwan Island. *Wea. Forecasting*, **26**, 44–60, https://doi.org/10.1175/2010waf2222386.1.

Livneh, B., P. J. Restrepo, and D. P. Lettenmaier, 2011: Development of a unified land model for prediction of surface hydrology and land–atmosphere interactions. *Journal of Hydrometeorology*, **12**, 1299–1320, https://doi.org/10.1175/2011JHM1361.1.

Luo, Y. H., and Y. Du, 2023: The roles of low-level jets in "21·7" Henan extremely persistent heavy rainfall event. *Adv. Atmos. Sci.*, **40**, 350–373, https://doi.org/10.1007/s00376-022-2026-1.

Luo, Y. L., and Coauthors, 2020: Science and prediction of heavy rainfall over China: Research progress since the reform and opening-up of new China. *J. Meteorol. Res.*, **34**, 427–459, https://doi.org/10.1007/s13351-020-0006-x.

Ma, R. Y., J. H. Sun, and X. L. Yang, 2021: A 7-yr climatology of the initiation, decay, and morphology of severe convective storms during the warm season over North China. *Mon. Wea. Rev.*, **149**, 2599–2612, https://doi.org/10.1175/mwr-d-20-0087.1.

Mass, C., 1981: Topographically forced convergence in western Washington state. *Mon. Wea. Rev.*, **109**, 1335–1347, https://doi.org/10.1175/1520-0493(1981)109<1335:tfciww>2.0.co;2.

Neiman, P. J., F. M. Ralph, A. B. White, D. E. Kingsmill, and P. O. G. Persson, 2002: The statistical relationship between upslope flow and rainfall in California's coastal mountains: Observations during CALJET. *Mon. Wea. Rev.*, **130**, 1468–1492, https://doi.org/10.1175/1520-0493(2002)130<1468:TSRBUF>2.0.CO;2.

Rojas, Y., and J. R. Minder, 2024: Variability of the Southern Andes rain shadow. *Atmospheric Research*, **308**, 107509, https://doi.org/10.1016/j.atmosres.2024.107509.

Siler, N., G. Roe, and D. Durran, 2013: On the dynamical causes of variability in the rain-shadow effect: A case study of the Washington cascades. *Journal of Hydrometeorology*, **14**, 122–139, https://doi.org/10.1175/jhm-d-12-045.1.

Skamarock, W. C., and Coauthors, 2019: A description of the advanced research WRF model version 4. NCAR Technical Note NCAR/TN-556+STR.

Smith, R. B., 1979: The influence of mountains on the atmosphere. *Advances in Geophysics*, **21**, 87–230, https://doi.org/10.1016/S0065-2687(08)60262-9.

Smith, R. B., 2019: 100 years of progress on mountain meteorology research. *Meteor. Monogr.*, **59**, 20.1–20.73, https://doi.org/10.1175/amsmonographs-d-18-0022.1.

Smith, R. B., and Coauthors, 2012: Orographic precipitation in the tropics: The Dominica experiment. *Bull. Amer. Meteor. Soc.*, **93**, 1567–1579, https://doi.org/10.1175/bams-d-11-00194.1.

Sun, J. S., 2005: A study of the basic features and mechanism of boundary layer jet in Beijing area. *Chinese Journal of Atmospheric Sciences*, **29**, 445–452, https://doi.org/10.3878/j.issn.1006-9895.2005.03.12. (in Chinese with English abstract)

Sun, J. S., and B. Yang, 2008: Meso-β scale torrential rain affected by topography and the urban circulation. *Chinese Journal of Atmospheric Sciences*, **32**, 1352–1364, https://doi.org/10.3878/j.issn.1006-9895.2008.06.10. (in Chinese with English abstract)

Thompson, G., P. R. Field, R. M. Rasmussen, and W. D. Hall, 2008: Explicit forecasts of winter precipitation using an improved bulk microphysics scheme. Part II: Implementation of a new snow parameterization. *Mon. Wea. Rev.*, **136**, 5095–5115, https://doi.org/10.1175/2008MWR2387.1.

Weckwerth, T. M., J. W. Wilson, M. Hagen, T. J. Emerson, J. O. Pinto, D. L. Rife, and L. Grebe, 2011: Radar climatology of the COPS region. *Quart. J. Roy. Meteor. Soc.*, **137**, 31–41, https://doi.org/10.1002/qj.747.

Weckwerth, T. M., and Coauthors, 2004: An overview of the international H_2O project (IHOP_2002) and some preliminary highlights. *Bull. Amer. Meteor. Soc.*, **85**, 253–278, https://doi.org/10.1175/BAMS-85-2-253.

Wilson, J. W., Y. R. Feng, M. X. Chen, and R. D. Roberts, 2010: Nowcasting challenges during the Beijing olympics: Successes, failures, and implications for future nowcasting systems. *Wea. Forecasting*, **25**, 1691–1714, https://doi.org/10.1175/2010waf2222417.1.

Wolyn, P. G., and T. B. Mckee, 1994: The mountain-plains circulation east of a 2-km-high north–south barrier. *Mon. Wea. Rev.*, **122**, 1490–1508, https://doi.org/10.1175/1520-0493(1994)122<1490:tmpceo>2.0.co;2.

Wu, F., and K. Lombardo, 2023: The impact of offshore-propagating squall lines on coastal-mountain flows. *Geophys. Res. Lett.*, **50**, e2023GL102825, https://doi.org/10.1029/2023GL102825.

Wu, Y. F., P. X. Li, and H. M. Chen, 2023: The characteristic and seasonal variation of mesoscale convective systems' precipitation over North China. *Quart. J. Roy. Meteor. Soc.*, **149**, 2348–2366, https://doi.org/10.1002/qj.4510.

Xiao, X., J. Z. Sun, M. X. Chen, X. Qie, Y. C. Wang, and Z. M. Ying, 2017: The characteristics of weakly forced mountain-to-plain precipitation systems based on radar observations and high-resolution reanalysis. *J. Geophys. Res.: Atmos.*, **122**, 3193–3213, https://doi.org/10.1002/2016JD025914.

Xiao, X., J. Z. Sun, M. X. Chen, X. Qie, Z. M. Ying, Y. C. Wang, and L. Ji, 2019: Comparison of environmental and mesoscale characteristics of two types of mountain-to-plain precipitation systems in the Beijing region, China. *J. Geophys. Res.: Atmos.*, **124**, 6856–6872, https://doi.org/10.1029/2018jd029896.

Xiao, X., J. Z. Sun, C. Y. Xu, Z. M. Ying, J. Li, L. N. Zhang, and M. X. Chen, 2025: Initiation of a record-breaking rainfall event in Beijing, China, associated with a penetrating inland sea-breeze front. *Mon. Wea. Rev.*, **153**, 2353–2374, https://doi.org/10.1175/MWR-D-24-0194.1.

Yang, H. P., and Y. Du, 2024: Difference between upshear- and downshear-propagating waves associated with the development of squall lines. *Mon. Wea. Rev.*, **152**, 1399–1420, https://doi.org/10.1175/MWR-D-23-0109.1.

Yang, H. P., and Y. Du, 2026: Distinct convection initiation near and far ahead of an idealized squall line. *J. Atmos. Sci.*, **83**, 151–168, https://doi.org/10.1175/JAS-D-25-0073.1.

Yin, S. Q., W. J. Li, D. L. Chen, J.-H. Jeong, and W. L. Guo, 2011: Diurnal variations of summer precipitation in the Beijing area and the possible effect of topography and urbanization. *Adv. Atmos. Sci.*, **28**, 725–734, https://doi.org/10.1007/s00376-010-9240-y.

Yu, R. C., T. J. Zhou, A. Y. Xiong, Y. J. Zhu, and J. M. Li, 2007: Diurnal variations of summer precipitation over contiguous China. *Geophys. Res. Lett.*, **34**, 2006GL028129, https://doi.org/10.1029/2006GL028129.